The influence of horizontal boundaries on Ekman circulation and angular momentum transport in a cylindrical annulus*

Aleksandr V Obabko[1], Fausto Cattaneo[1,2] and Paul F Fischer[2]

[1] Department of Astronomy and Astrophysics, University of Chicago, Chicago, IL 60637, USA
[2] Division of Mathematics and Computer Science, Argonne National Laboratory, Argonne, IL 60439, USA

E-mail: obabko@uchicago.edu

Abstract
We present numerical simulations of circular Couette flow in axisymmetric and fully three-dimensional geometry of a cylindrical annulus inspired by Princeton magnetorotational instability (MRI) liquid gallium experiment. The incompressible Navier–Stokes equations are solved with the spectral element code Nek5000 incorporating realistic horizontal boundary conditions of differentially rotating rings. We investigate the effect of changing rotation rates (Reynolds number) and of the horizontal boundary conditions on flow structure, Ekman circulation and associated transport of angular momentum through the onset of unsteadiness and three-dimensionality. A mechanism for the explanation of the dependence of the Ekman flows and circulation on horizontal boundary conditions is proposed.

PACS numbers: 47.32.Ef, 47.11.Kb, 02.70.Jn

(Some figures in this article are in colour only in the electronic version.)

1. Introduction

The phenomenon of Ekman circulation (EC) occurs in most if not all rotating flows with stressed boundaries that are not parallel to the axis of rotation. The manifestation of EC ranges from wind-driven ocean currents (Batchelor 1967) to the accumulation of the tea leaves at the bottom of a stirred cup (see e.g. Alpher and Herman 1960). One of the consequences of EC and of the associated Ekman flows is to greatly enhance mixing and transport and, in particular, the transport of angular momentum, above the values due to viscosity alone. Traditionally, Ekman flows are explained in terms of action of Coriolis forces in the Ekman layers along the rotating stressed boundaries (Greenspan 1968).

There are circumstances when the presence of EC has undesirable effects. For example, this is the case in

laboratory experiments for studying the development of magnetorotational instability (MRI) in liquid metals (see the monograph edited by Rosner *et al* 2004). The MRI is important in astrophysics where it is believed to lead to turbulence in magnetized accretion disks (Balbus 2003). Many of the features of MRI and its associated enhancement of angular momentum transport (AMT) can be studied experimentally in magnetized flows between rotating coaxial cylinders. In these experiments, the rotation rates of the cylinders are chosen in such a way that the fluid's angular momentum increases outwards so that the resulting rotational profile is stable to axisymmetric perturbations (the so-called centrifugally stable regime). The presence of a weak magnetic field can destabilize the basic flow, provided the angular velocity increases inward, and lead to an enhancement of outward AMT.

In an ideal situation, the basic state consists of circular Couette flow (CCF), and the outward transport of angular momentum in the absence of magnetic fields is solely due

---

to viscous effects. The presence of a magnetic field would destabilize the basic flow through the effects of MRI and lead to a measurable increase of AMT. In practice, this ideal case can never be realized in laboratory experiments because of horizontal boundaries. The presence of these boundaries drives an EC that enhances AMT even in the absence of magnetic effects. In order to study the enhancement of AMT due to MRI, it is crucial to be able to distinguish the effects that are magnetic in origin from those that are due to the EC. One possibility is to make the cylinders very tall so the horizontal boundaries are far removed from the central region. This approach, however, is not practical owing to the high price of liquid metals.

The alternative approach is to devise boundaries in such a way that the resulting EC can be controlled and possibly reduced. for example, attaching the horizontal boundaries to the inner or outer cylinder results in dramatically different flow patterns. Another possibility is to have the horizontal boundaries rotating independently of the inner and outer cylinders. Goodman, Ji and coworkers (Kageyama *et al* 2004, Burin *et al* 2006, Ji *et al* 2006) have proposed to split the horizontal boundaries into two independently rotating rings whose rotational speeds are chosen so as to minimize the disruption to the basic CCF by secondary ECs. Indeed this approach has been implemented in the Princeton's MRI liquid gallium experiment (Schartman 2008). In any case, no matter how the horizontal boundaries are implemented it is important to understand what kind of EC pattern arises before the magnetic effects are introduced.

In the present paper, we address this issue by studying the effects of horizontal boundary conditions on CCF numerically. We study both axisymmetric and fully three-dimensional (3D) geometries and investigate the effects of changing rotation rates (Reynolds number) through the onset of unsteadiness and three-dimensionality. The next section (section 2) describes the formulation of the problem and gives an account of numerical aspects of its solution technique including a brief description of the spectral element code Nek5000 (Fischer *et al* 2008). Section 3 starts with an explanation of flow behavior due to horizontal boundary conditions, i.e. CCF, EC and disrupted EC due to periodic horizontal boundaries, 'lids' and 'rings', correspondingly (section 3.1). Then the paper proceeds with a description of the comparison of our results with the experimental data (section 3.2) followed by an examination of torque and AMT (section 3.3). Finally, we draw conclusions and describe future work in section 4.

2. Problem formulation and numerical method

2.1. Formulation

We study the flow of an incompressible fluid with finite (constant) kinematic viscosity ν in a cylindrical annulus bounded by coaxial cylinders. The cylinders have the radii R_1^* and R_2^* ($R_1^* < R_2^*$) and rotate with angular velocities Ω_1^* and Ω_2^*, respectively. The annulus is confined in the vertical direction by horizontal boundaries at distance H^* apart. The formulation of the problem in cylindrical coordinates (r, θ, z) with the scales for characteristic length L and velocity U,

$$L = R_2^* - R_1^*, \qquad U = \Omega_1^* R_1^* - \Omega_2^* R_2^* \qquad (1)$$

and therefore with the relationship between dimensional variables (with asterisk) and non-dimensional radius, height, velocity vector $\boldsymbol{V}$, time and pressure given by

$$[r^*, z^*, \boldsymbol{V^*}, t^*, p^*] = \left[L\, r, L\, z, U\boldsymbol{V}, \frac{L}{U}\, t, \rho U^2 p \right] \qquad (2)$$

correspondingly, results in the following non-dimensional incompressible Navier–Stokes equations:

$$\frac{\partial V_r}{\partial t} + (\boldsymbol{V} \cdot \boldsymbol{\nabla})\, V_r - \frac{V_\theta^2}{r} = \frac{1}{Re} \left[\triangle V_r - \frac{2}{r^2} \frac{\partial u_\theta}{\partial \theta} - \frac{V_r}{r^2} \right] - \frac{\partial p}{\partial r}, \qquad (3)$$

$$\frac{\partial V_\theta}{\partial t} + (\boldsymbol{V} \cdot \boldsymbol{\nabla})\, V_\theta + \frac{V_r V_\theta}{r}$$
$$= \frac{1}{Re} \left[\triangle V_\theta + \frac{2}{r^2} \frac{\partial u_r}{\partial \theta} - \frac{V_\theta}{r^2} \right] - \frac{1}{r} \frac{\partial p}{\partial \theta}, \qquad (4)$$

$$\frac{\partial V_z}{\partial t} + (\boldsymbol{V} \cdot \boldsymbol{\nabla})\, V_z = \frac{1}{Re} \triangle V_z - \frac{\partial p}{\partial z}, \qquad (5)$$

$$\frac{\partial V_r}{\partial r} + \frac{1}{r} \frac{\partial V_\theta}{\partial \theta} + \frac{\partial V_z}{\partial z} + \frac{V_r}{r} = 0, \qquad (6)$$

where ρ is a constant fluid density and Reynolds number Re is defined as

$$Re = \frac{UL}{\nu} = \frac{(\Omega_1^* R_1^* - \Omega_2^* R_2^*)(R_2^* - R_1^*)}{\nu}, \qquad (7)$$

while the scalar advection operator due to a vector field $\boldsymbol{V}$ and Laplacian of a scalar function $S(r, z)$ are given by

$$(\boldsymbol{V} \cdot \boldsymbol{\nabla})\, S = V_r \frac{\partial S}{\partial r} + \frac{V_\theta}{r} \frac{\partial S}{\partial \theta} + V_z \frac{\partial S}{\partial z},$$
$$\triangle S = \frac{\partial^2 S}{\partial r^2} + \frac{1}{r} \frac{\partial S}{\partial r} + \frac{1}{r^2} \frac{\partial^2 S}{\partial \theta^2} + \frac{\partial^2 S}{\partial z^2}. \qquad (8)$$

The initial conditions for the flow in the annulus and boundary conditions at the cylinder surfaces $r = R_1$ and $r = R_2$ are

$$V_r = V_z = 0, \qquad V_\theta = r\, \Omega(r), \qquad (9)$$

where non-dimensional angular velocity $\Omega(r)$ is given by CCF profile

$$\Omega_{\rm C}(r) = A + \frac{B}{r^2},$$
$$A = \frac{\Omega_2 R_2^2 - \Omega_1 R_1^2}{R_2^2 - R_1^2}, \qquad (10)$$
$$B = \frac{R_1^2 R_2^2 (\Omega_1 - \Omega_2)}{R_2^2 - R_1^2}.$$

At the horizontal boundaries $z = 0$ and $z = H$, two types of the boundary conditions have been considered, namely, *lids* and *rings*, given by (9) where angular velocity $\Omega(r)$ is equal to

$$\Omega(r) = \begin{cases} \Omega_1 & : \quad r = R_1, \\ \Omega_3 & : \quad R_1 < r < R_{12}, \\ \Omega_4 & : \quad R_{12} < r < R_2, \\ \Omega_2 & : \quad r = R_2. \end{cases} \qquad (11)$$

Here R_{12} is the radial location of the boundary between the inner and outer rings, and Ω_3 and Ω_4 are angular velocities of the inner and outer rings, correspondingly. Inspired by the Princeton MRI liquid gallium experiment (Schartman 2008), the non-dimensional angular velocities and cylinder height as well as the cylinder and ring boundary radii used in this study are given in table 1 in addition to the dimensional parameters involved in comparison with the experiment (subsection 3.2). In the cases with lids, angular velocities Ω_3 and Ω_4 are equal to the angular velocity of the outer cylinder Ω_2, whereas in the cases with rings, they turn out to be close to the values of CCF profile (10) taken at the middle of radii of the corresponding rings.

2.2. Numerical technique

The axisymmetric version of equations (3)–(6) and the fully 3D version in Cartesian coordinates have been solved numerically with the spectral-element code Nek5000 developed and supported by Paul Fischer and coworkers (see Fischer *et al* 2007, 2008, and references therein).
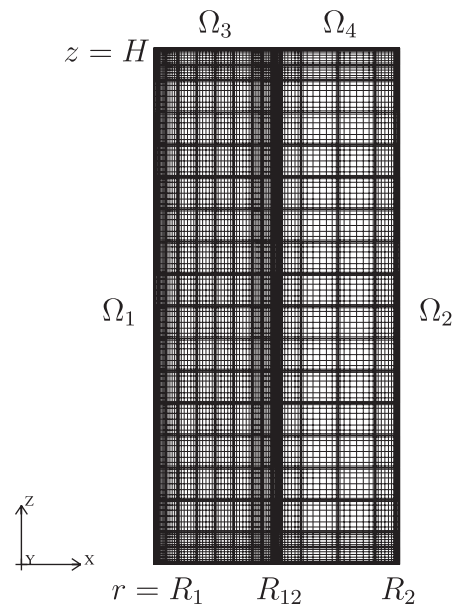
The temporal discretization in Nek5000 is based on a semi-implicit formulation in which the nonlinear terms are treated explicitly in time and all remaining linear terms are treated implicitly. In particular, we used a combination of either kth-order backward difference formula (BDFk) for the diffusive/solenoidal terms with extrapolation (EXT$k-1$) for the nonlinear terms or the operator-integration factor scheme (OIFS) method where BDFk is applied to the material derivative, with the explicit fourth-order Runge–Kutta scheme being used for the resulting pure advection initial value problem.

With either the BDFk/EXT$k-1$ or OIFS approach, the remaining linear portion of time advancement amounts to solving an unsteady Stokes problem. This problem is first discretized spatially using the spectral-element method (SEM) and then split into independent subproblems for the velocity and pressure in weak variational form. The computational domain is decomposed into K non-overlapping subdomains or elements, and within each element, unknown velocity and pressure are represented as the tensor-product cardinal Lagrange polynomials of the order N and $N-2$, correspondingly, based at the Gauss–Lobatto–Legendre (GLL) and Gauss–Legendre (GL) points. This velocity–pressure splitting and GLL–GL grid discretization requires boundary condition only for velocity field and avoids an ambiguity with the pressure boundary conditions in accordance with the continuous problem statement.

The discretized Stokes problem for the velocity update gives a linear system which is a discrete Helmholtz operator. It comprises the diagonal spectral element mass matrix with spectral element Laplacian being strongly diagonally dominant for small time steps, and therefore, Jacobi (diagonally) preconditioned conjugate gradient iteration is readily employed. Then the projection of the resulting trial viscous update on divergence-free solution space enforces the incompressibility constraint as the discrete pressure Poisson equation is solved by conjugate gradient iteration preconditioned by either the two-level additive Schwarz

Table 1. The geometry and rotation parameters for the computational cases with lids and rings at $Re = 6190$ and the experimental setup with lids at $Re = 9270$, along with the drawing of the cut of 3D computational mesh at $\theta = 0$ for the case with rings. Note the clustering of the grid lines at the boundaries of the spectral elements whose location and dimensions are chosen to resolve efficiently boundary layers and 'step' changes in angular velocity between cylinders and rings.

	Lids		Rings	Experiment: Lids	
R_1		0.538		R_1^* (cm)	7.1
R_2		1.538		R_2^* (cm)	20.3
R_{12}		1.038		R_{12}^* (cm)	13.7
H		2.114		H^* (cm)	27.9
Ω_1		3.003		Ω_1^* (rpm)	200
Ω_2	0.488		0.400	Ω_2^* (rpm)	26
Ω_3	0.488		1.367	Ω_3^* (rpm)	26
Ω_4		0.488		Ω_4^* (rpm)	26

method or hybrid Schwarz/multigrid methods. Note that we used dealising/overintegration where the oversampling of polynomial order by a factor of 3/2 was made for the exact evaluation of quadrature of inner products for nonlinear (advective) terms.

The typical axisymmetric case with rings at high Reynolds number of $Re = 6200$ (see figure 4(b)) required the spacial resolution with polynomial order $N = 10$ and number of spectral elements $K = 320$ (cf drawing for table 1) and was computed with time step $\Delta t = 10^{-3}$ for the duration of $t \sim 300$, whereas the axisymmetric run with lids at the same Re (figure 4(a)) had $N = 8$, $K = 476$, $\Delta t = 5 \times 10^{-3}$ and $t \sim 500$. The corresponding 3D cases with rings and lids had $N = 11$, $K = 9600$, $\Delta t = 6.25 \times 10^{-4}$ and $t \sim 280$ and $N = 9$, $K = 14280$, $\Delta t = 6.25 \times 10^{-4}$ and $t \sim 180$, respectively. Note that in order to facilitate time advancement and minimize CPU requirements, the final output from other cases, e.g. with lower Reynolds number Re, was used as the initial conditions for some of the computations with higher Re, and the corresponding axisymmetric cases with small random non-axisymmetric perturbation were a starting point for most of our fully 3D computations. Apart from CPU savings, the usage of the perturbed axisymmetric solution obtained in *cylindrical formulation* (3–6) as the initial condition

for 3D computations at low Reynolds numbers ($Re = 620$) served as an additional validation of the code setup because of the convergence of the fully 3D results computed in *Cartesian formulation* back to the unperturbed axisymmetric steady-state initial condition (see also subsection 3.3).

Finally, the step change of angular velocities that mimics its transition in the gaps or grooves between the cylinders and horizontal boundaries as well as between the inner and outer rings in the Princeton MRI liquid gallium experiment (Schartman 2008) was modelled within one spectral element of the radial size $L_g = 0.020$ by ramping power law function of radius with an exponent that was varied in the range from 4 to $N - 1$ without noticeable effect on the flow.

3. Results

Let us first start with examination of the effects of horizontal boundary conditions on flow pattern in general and EC in particular before moving to a comparison with the experiment and examination of angular momentum transport in the cylindrical annulus.

3.1. Horizontal boundary effects

Here, we contrast two types of horizontal boundary conditions with an ideal baseline case of CCF. Being zero in the ideal case, we argue that the imbalance between 'centrifugal' rotation and centripetal pressure gradient determines the fate of the radial flow along horizontal boundaries in the cylindrical annulus.

In the ideal case of CCF, the sheared circular motion is balanced by centripetal pressure gradient. To be precise, the ideal CCF is the following exact solution of equations (3)–(6) for periodic (or stress-free) horizontal boundary conditions:

$$V_r = V_z = 0, \qquad V_\theta = r\Omega_C(r) = Ar + \frac{B}{r}, \tag{12}$$

$$p_C(r) = \int^r \frac{V_\theta^2}{r}\,dr = \frac{A^2 r^2}{2} - \frac{B^2}{2r^2} + 2AB \log r + \text{const}.$$

Here, the constant A given by equation (10) is proportional to the increase in axial angular momentum,

$$\mathcal{L} = rV_\theta = \Omega r^2 \tag{13}$$

outward between the cylinders, whereas the constant B is set by shear-generating angular velocity drop between them. Figure 1 shows CCF azimuthal velocity V_θ (dashed), angular velocity Ω_C (solid), axial angular momentum $\mathcal{L}$ (dashed–dotted) and negative of pressure $-p_C$ (dotted) for the non-dimensional parameters given in table 1. Since we are primarily interested in further MRI studies, the baseline flow has to be centrifugally stable, i.e. with angular momentum $\mathcal{L}$ increasing outward (for $\Omega > 0$), and therefore, satisfying the Rayleigh criterion

$$\frac{\partial \mathcal{L}^2}{\partial r} > 0, \tag{14}$$

which is the case in this ideal CCF (dashed–dotted line in figure 1). In order to maintain rotation with shear in this virtual
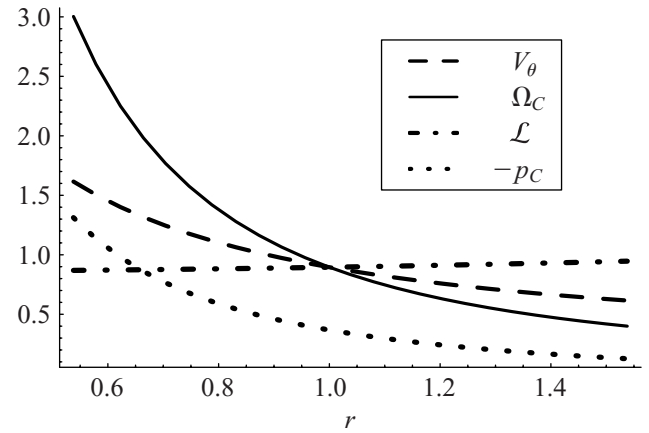

Figure 1. The CCF azimuthal velocity V_θ ($- - -$), angular velocity Ω_C (——), axial angular momentum $\mathcal{L} = rV_\theta$ (— · —) and minus pressure P_C (· · · · · ·) versus radius. Note the monotonically increasing angular momentum and decreasing angular velocity with radius for centrifugally stable CCF where the 'centrifugal' rotation balances the centripetal pressure gradient leading to zero radial and axial velocities.

experiment with periodic horizontal boundaries, the positive axial torque $\mathcal{T}_C$

$$\begin{aligned}
\mathcal{T}_C &= \int_A \left(\vec{r} \times (d\vec{A} \cdot \boldsymbol{\tau}) \right)_z \\
&= \int_0^H \int_0^{2\pi} dz\, d\theta\, \frac{r^3}{Re} \frac{\partial}{\partial r} \frac{V_\theta}{r}\bigg|_{V_\theta = r\Omega_C} \\
&= \frac{4\pi H R_1^2 R_2^2}{R_2^2 - R_1^2} \frac{\Omega_1 - \Omega_2}{Re}
\end{aligned} \tag{15}$$

has to be applied to the inner cylinder while the outer cylinder is kept from shear-free solid body rotation ($\Omega(r) = \Omega_1 = A$, $B = \mathcal{T} = 0$) by negative torque $-\mathcal{T}_C$. Note that in the above equation (15), $\boldsymbol{\tau}$ is the non-dimensional shear stress tensor (see also appendix B).

3.1.1. EC with 'lids'. In practice, the ideal CCF can never be realized in laboratory experiments because of horizontal boundaries. The simplest realizable configuration is the one we refer to as 'lids' when horizontal boundaries are coupled to the outer cylinder ($\Omega_3 = \Omega_4 = \Omega_2$). To see how flow changes in the presence of lids that rotate with the outer cylinder, let us imagine that these lids were inserted impulsively into fluid with ideal CCF profile given by equation (12) and plotted as a solid line in figure 1 for Ω_1 and Ω_2 from table 1. Keeping the most important terms in the axisymmetric form of equation (3) gives

$$\frac{\partial V_r}{\partial t} = \Omega^2 r - \frac{\partial p}{\partial r} + \frac{1}{Re} \frac{\partial^2 V_r}{\partial z^2} + \cdots, \tag{16}$$

where we have used $V_\theta = r\Omega$. For the initial condition of CCF (12), the left-hand side of equation (16) is equal to zero everywhere outside the lids, which is also consistent with zero radial flow $V_r = 0$. This zero radial flow also results in zero diffusion term $\frac{1}{Re} \frac{\partial^2 V_r}{\partial z^2}$ in equation (16) and zero net radial force $\Omega^2 r - \frac{\partial p}{\partial r}$. The latter results from the exact CCF balance between (positive) 'centrifugal' rotation term $\Omega_C^2 r$ and (negative) centripetal pressure gradient term $-\frac{\partial p}{\partial r}$ in equation (16).
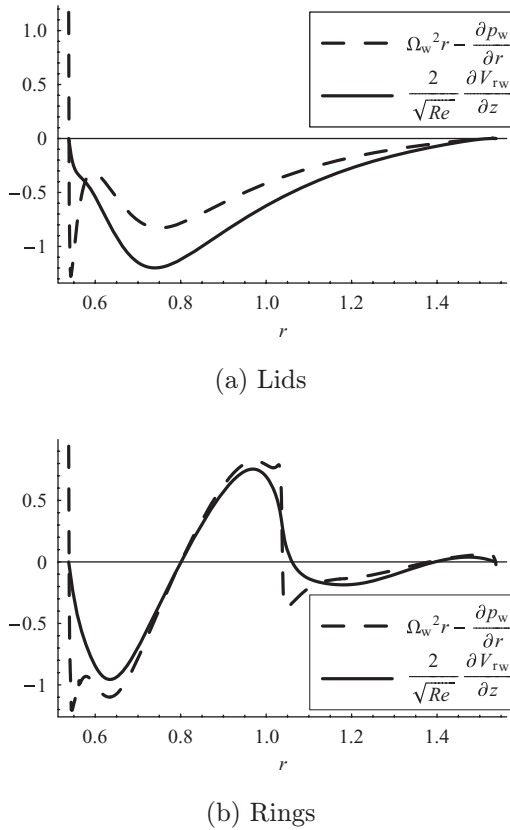
4

(a) Lids

(b) Rings

Figure 2. Steady-state scaled radial wall shear (——) and near-wall net radial force (– – –) for $Re = 620$ in the case of lids (a) and rings (b). The definite negative net radial force in the lids case (a) results in the inward radial Ekman flow with negative radial wall shear being disrupted in the case of rings (b) by the alternating sign of the net radial force that correlates well with the sign of the wall shear and thus with the alternating directions of Ekman flows.

Instead of initial ideal CCF angular velocity Ω_C (12), the flow next to the lids now rotates with a smaller angular velocity of the outer cylinder ($\Omega_2 = \Omega_3 = \Omega_4 < \Omega_C$). However, the centripetal pressure gradient is still set by the bulk rotation of the rest of the fluid and therefore becomes suddenly larger than the 'centrifugal' rotation of fluid next to the lids, i.e. $\frac{\partial p}{\partial r} = \Omega_C^2 r > \Omega^2 r$. As a result of this angular momentum deficit of near-wall fluid, the centripetal pressure gradient prevails over rotation term in (16). Therefore, the net radial force becomes nonzero and negative, $\Omega^2 r - \frac{\partial p}{\partial r} < 0$, resulting in negative sign of $\frac{\partial V_r}{\partial t}$ (16) and, therefore, in the formation of the Ekman layer with an inward radial flow ($V_r < 0$) in the vicinity of the lids.

Figure 2(a) confirms that the net radial force near e.g. the lower horizontal surface $z = 0$, $\Omega_2^2 r - \frac{\partial p}{\partial r}|_{z=0}$ (dashed) is negative, as well as the scaled poloidal wall shear $\frac{2}{\sqrt{Re}} \frac{\partial V_r}{\partial z}|_{z=0}$. The latter means that the z-derivative of V_r is negative at the lower lid, which in turn results in a decrease of radial velocity with the increase of height z from noslip zero value at the lid, $V_r|_{z=0} = 0$ (9), to negative values associated with the inward Ekman flow. Thus the deficit of angular momentum in the near-wall fluid of the Ekman layer results in unbalanced centripetal pressure gradient set by the bulk rotation of the rest of the flow outside the layer and drives the Ekman flow radially inward.
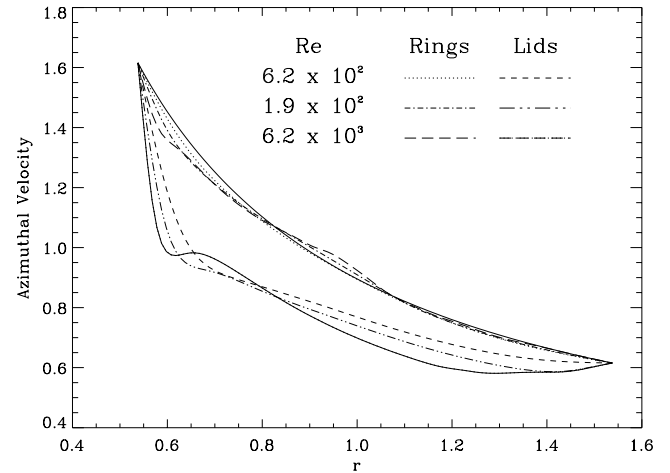

Figure 3. Azimuthal velocity V_θ versus radius for the circular Couette flow (——) and instantaneous axisymmetric profiles at $z = \frac{H}{4}$ in the case of lids for the series of Reynolds numbers $Re = 620$ (- - - -), 1900 (dash-triple-dot) and 6200 (— · —), and in the case of rings for the same Reynolds numbers: (· · · · · ·), (— · —) and (– – –), respectively. The EC-induced momentum deficiency in azimuthal velocity profiles in the cases with lids is greatly diminished by the particular choice of angular velocities of independently rotating rings.

To summarize, the presence of slower rotating lids disrupts the initial ideal CCF equilibrium between centrifugal rotation and centripetal pressure gradient set by rotation of, respectively, the lids and bulk of the flow. This leads to the negative net radial force, $\Omega^2 r - \frac{\partial p}{\partial r} < 0$, and inward Ekman flow, $V_r < 0$, owing to $\frac{\partial V_r}{\partial t} < 0$. As time grows, so does the magnitude of negative radial velocity in the Ekman layer and, eventually, the diffusion term $\frac{1}{Re} \frac{\partial^2 V_r}{\partial z^2}$ (16) in the Ekman boundary layer of the width $\Delta z \sim O(\sqrt{Re})$ becomes of the same order (i.e. $\sim O(1)$) as the net radial force that results from two other terms in (16). Thus the diffusion effects finally balance the rotation momentum deficit of the fluid in Ekman boundary layers near the lids in the saturation steady state (see also appendix A).

To check consistency of this argument, the saturation magnitude of $\frac{\partial p}{\partial z}$ across the layer is verified to be more than an order of magnitude smaller than the corresponding $\frac{\partial p}{\partial r}$, which confirms that saturation centripetal pressure gradient $-\frac{\partial p}{\partial r}$ is indeed set by the bulk rotation of the fluid outside the Ekman boundary layers. The saturation bulk rotation can be illustrated by the instantaneous saturation profiles of azimuthal velocity shown in figure 3 for the steady cases with lids for $Re = 620$ (dashed) and 1800 (dash-triple-dot), and unsteady case with lids of $Re = 6200$ (dash-double-dot) at $z = \frac{H}{4}$. It is interesting that for the range of Reynolds numbers considered, the effect of the increase of Reynolds number is minor in comparison with significant azimuthal momentum deficiency that has resulted from the change of horizontal boundary conditions from initial ideal CCF (solid) to the cases of Ekman flows over lids.

Owing to momentum deficiency of the near-wall fluid, the higher centripetal pressure gradient drives the inward Ekman flows along the lids that result in EC in the cylindrical annulus. In order to further illustrate the phenomenon of EC due to horizontal boundaries, we have plotted the contours of
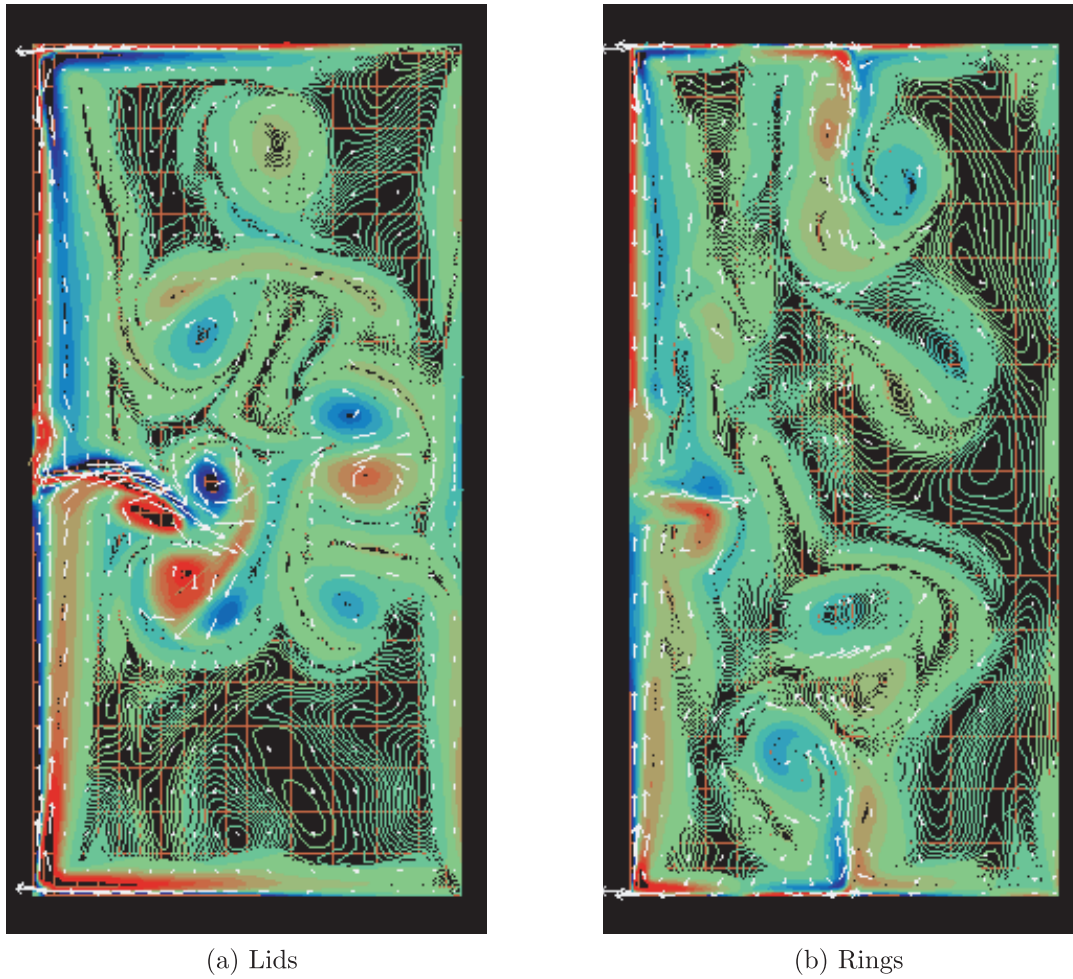
<table>
<tr><td>(a) Lids</td><td>(b) Rings</td></tr>
</table>

Figure 4. Instantaneous contours of azimuthal vorticity and vector field of poloidal velocity for $Re = 6200$ in the case of lids (a) and rings (b). The EC and outward radial jet near the midplane in the case of lids are severely disrupted in the setup with rings due to alternating inward–outward Ekman flows.

azimuthal vorticity ω_θ and vector plot of poloidal velocity (V_r, V_z) in figure 4(a) for the case of $Re = 6200$ with the former given by

$$\omega_\theta = \frac{\partial V_r}{\partial z} - \frac{\partial V_z}{\partial r}, \qquad \omega_\theta\Big|_{z=0} = \frac{\partial V_r}{\partial z}\Big|_{z=0},$$
$$\omega_\theta\Big|_{r=R_1} = -\frac{\partial V_z}{\partial r}\Big|_{r=R_1}, \tag{17}$$

where noslip conditions (9) along the walls have been used. Here the vorticity contours are coloured from blue ($\omega_\theta < 0$) to red ($\omega_\theta > 0$). Note that this change of colours from blue to red (through green colour whenever it is visible) shows the locus of zero vorticity that gives the approximate location of a jet or jet-like features in the flows along the lids at $z = 0$ or $z = H$ with extremum in V_r and in the flows along the cylinders at $r = R_1$ or $r = R_2$ with minimum or maximum in V_z (17). In figure 4(a), we observe the Ekman boundary layers along the lids with vorticity contours changing their colours from blue ($\omega_\theta < 0$) to red at the lower lid and from red ($\omega_\theta > 0$) to blue at the upper lid. In both instances, this change of colour shows the locus of minimum in $V_r < 0$ or the location where inward Ekman flow is the strongest. Similarly, the change of colours near the inner cylinder surface shows the opposing

vertical jet-like flows along the inner cylinder that merge near the midplane $z = H/2$ and, owing to continuity (6), form a strong outward radial jet. At these high Reynolds numbers, beyond $Re \sim 1800$, the radial jet becomes unsteady and starts to oscillate breaking into pairs of vortices or, to be precise, into pairs of vortex rings that move toward the lids drawn by the mass loss in the Ekman layers and thus closing the EC cycle.

Summing up the flow pattern in the case of lids, we conclude that because of the deficit of rotation momentum in Ekman layers, the fluid is pushed centripetally in these layers along the lids and further along the inner cylinder with the subsequent formation of the strong outward radial jet that eventually transports fluid back to the lids and closes the cycle of the EC (see also appendix A and section 3.3).

3.1.2. EC disruption due to 'rings'. When each horizontal boundary is split into a pair of rings that rotate independently with the angular velocities Ω_3 and Ω_4 (table 1), the bulk rotation and resulting centripetal pressure gradient are restored back to that of the CCF. The restored profiles of azimuthal velocity in the cases with rings are shown in figure 3 for the same Reynolds numbers as for the cases with lids, namely for the steady cases of $Re = 620$ (dotted) and 1800 (dash–dot) and unsteady case of $Re = 6200$ (long dash).

Along with the restoration of the bulk rotation back to that of the CCF, we observe other major differences between the cases with lids (a) and rings (b) in the flow field structure illustrated in figure 4.

Instead of a single outward radial jet and inward Ekman flows along the lids, figure 4(b) shows alternating inward–outward Ekman flows along the rings that, as we describe below, produce strong vertical jets near $r = R_{12}$ and a weaker outward radial jet near the midplane $z = H/2$. The alternating inward–outward Ekman flows along e.g. the lower inner and outer rings ($z = 0$) are also evident in figure 2(b) where the scaled poloidal shear $\frac{2}{\sqrt{Re}} \frac{\partial V_r}{\partial z}\big|_{z=0}$ (solid) is plotted as a function of radius for $Re = 620$. The radial locations of zero shear on the inner and outer rings, R_{s3} and R_{s4}, respectively, in this case are found to be

$$R_{s3} = 0.801, \quad R_{s4} = 1.395 \quad \text{such that}$$
$$\frac{\partial V_r}{\partial z}\big|_{(r,z)=(R_{si},0)} = 0, \qquad \text{where } i = 3, 4. \tag{18}$$

We observe that the scaled poloidal shear $\frac{2}{\sqrt{Re}} \frac{\partial V_r}{\partial z}\big|_{z=0}$ is negative between $r = R_1$ and $r = R_{s3}$ and between $r \approx R_{12}$ and $r = R_{s4}$. Similar to the case with lids (figure 2(a)), this negative z derivative of V_r means that $V_r < 0$ and the Ekman flow along these portions of rings is directed radially inward. Likewise, the positive radial velocity or outward Ekman flow between $r = R_{s3}$ and $r \approx R_{12}$ and between $r = R_{s4}$ and $r = R_2$ corresponds to positive poloidal shear in figure 2(b). Furthermore, as in the case of lids (figure 2(a)), the signs and zeros of the scaled poloidal shear and radial velocity correlate well with that of the net radial force $\Omega^2 r - \frac{\partial p}{\partial r}$ (dashed line in figure 2(b)). In addition, these radial locations of the reversals of net radial force and of Ekman flows near $r = R_{s3}$ and $r = R_{s4}$ (12) coincide within up to 2% with the radial locations R_3 and R_4 where the ideal CCF angular velocity (12) matches the angular velocity of the inner and outer rings Ω_3 and Ω_4 (table 1), namely

$$R_3 = 0.793, \quad R_4 = 1.369, \quad \text{such that}$$
$$\Omega_i = \Omega_C(R_i), \qquad \text{where } i = 3, 4. \tag{19}$$

This strong correlation of reversals of the net radial force with reversals of Ekman flow at $r = R_{s3}$ and $r = R_{s4}$ (18), coinciding with local CCF rotation at $r = R_3 \approx R_{s3}$ and $r = R_4 \approx R_{s4}$, is completely consistent with our argument that the balance and imbalance between 'centrifugal' rotation and centripetal pressure gradient determines the fate of the radial flow along horizontal boundaries. Namely, the zero radial velocity at $r = R_{s3}$ and $r = R_{s4}$ results from the CCF-like balance of centripetal pressure gradient $-\frac{\partial p}{\partial r}$ and 'centrifugal' rotation $\Omega^2 r \approx \Omega_C^2 r$ (12) since $R_3 \approx R_{s3}$ and $R_4 \approx R_{s4}$ (equations (18) and (19)). Moreover, a monotonic decrease of Ω_C (12) with increase of r (solid line in figure 1) means that the near-wall fluid rotation at angular velocities of the rings Ω_3 and Ω_4 is locally slower (faster) than that of CCF for the radius r that is smaller (bigger) than $r \approx R_{s3}$ and $r \approx R_{s4}$, correspondingly. Thus near-wall fluid rotation momentum deficit (excess) results, respectively, in the negative (positive) sign of the net radial force $\Omega^2 r - \frac{\partial p}{\partial r}$

and, therefore, negative (positive) sign of radial velocity V_r in figure 4(b) and poloidal shear $\frac{2}{\sqrt{Re}} \frac{\partial V_r}{\partial z}\big|_{z=0}$ in figure 2(b) for the radial location r that is smaller (larger) than $r \approx R_{s3}$ and $r \approx R_{s4}$.

In summary, the angular velocities of the inner and outer rings (Ω_3 and Ω_4) set the CCF-like equilibrium radii ($r \approx R_{s3}$ and $r \approx R_{s4}$) by matching locally to monotonically decreasing CCF-like profile of bulk flow rotation. The near-wall fluid over the portions of the rings that have a smaller radius r than these CCF equilibrium radii experiences rotation momentum deficit that results in the inward Ekman flows due to locally higher centripetal pressure gradient set by faster bulk rotation as in the cases with lids. Conversely, when $r > R_{s3}$ and $r > R_{s4}$, the bulk rotation is slower than the near-wall velocity because of monotonic decrease of velocity profile with increase of radius outside the Ekman layers, and the fluid has enough near-wall rotation momentum to overcome centripetal pressure gradient and to drive the outward Ekman flows as observed in figure 4(b).

The rest of the prominent features of the flow field in figure 4(b) like the strong vertical jets near $r = R_{12}$ and a weak outward radial jet near the midplane $z = H/2$ are the direct consequences of these alternating inward–outward Ekman flows along the rings. Namely, driven by rotation momentum excess and deficit of fluid near the inner and outer rings, respectively, pairs of opposing Ekman flows along both horizontal boundaries merge near the boundary between the inner and outer rings $r = R_{12}$. Owing to continuity (6), these pairs of colliding Ekman flows with, presumably, equal linear radial momentum launch the opposing vertical jets near the ring boundary $r = R_{12}$ that become unsteady with the increase of Reynolds number and break into vortex pairs or vortex rings. Similarly, the Ekman flows along lower and upper inner rings due to the rotation momentum deficit are pushed into the corners with the inner cylinder and further along the inner cylinder until they merge near the midplane $z = H/2$ to form an outward radial jet as in the case with lids. But contrary to the cases with lids, the outward radial jet is now significantly weaker owing to the fact that the effective Reynolds number for these flows are smaller than in the cases with lids due to the smaller characteristic length scale ($R_{s3} - R_1 < L$) and velocity scale ($\Omega_3 R_{s3} - \Omega_1 R_1 < U$), which leads to larger Ekman numbers $E = \frac{\nu}{\Delta\Omega L^2} = \frac{U/(\Delta\Omega L)}{Re}$.

Finally, we would like to make the following two comments. Firstly, 3D effects appear to be negligible at these Reynolds numbers with the only noteworthy difference of considerably shorter vertical jets near the ring boundary $r = R_{12}$ as compared with the axisymmetric cases. Secondly, the angular velocities of rings control the angle and direction of the jet near this ring boundary $r = R_{12}$. In particular, when rings are coupled together and rotate with the outer cylinder ('lids'), the jets become the inward Ekman flows along the lower and upper horizontal boundaries so that the angle with radius vector is $\pm\pi$, correspondingly. When rings are decoupled and rotate with the angular velocities considered above (table 1), the Ekman flows collide near the ring boundary $r = R_{12}$ and launch the opposing vertical jets, i.e. the angle is $\pm\pi/2$. When rings are coupled to the inner cylinder, we have checked that the resulting Ekman flows have radially outward direction due to the excess of the near-wall
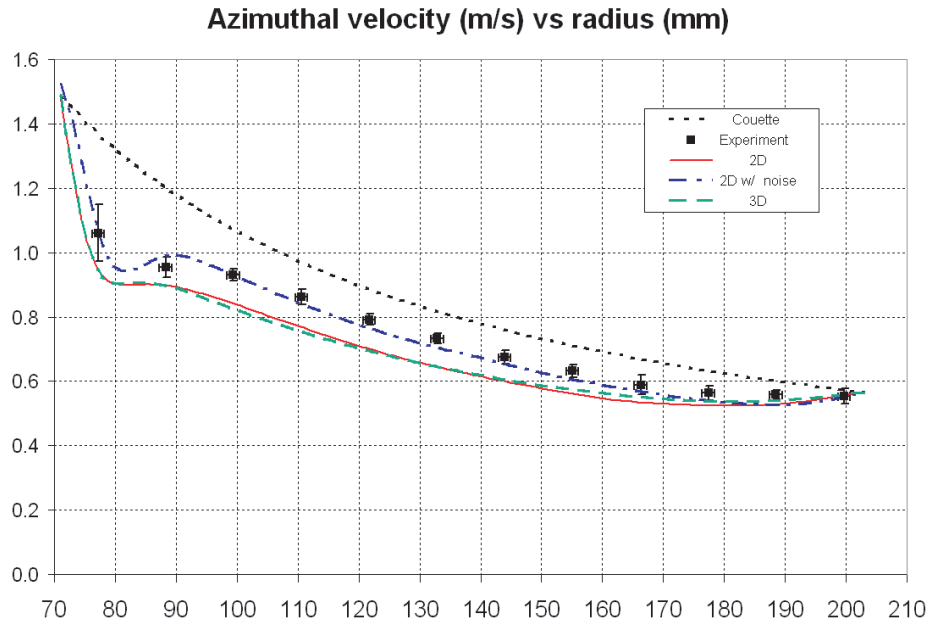
Azimuthal velocity (m/s) vs radius (mm)

Figure 5. Dimensional azimuthal velocity profile versus radius at $z = \frac{H}{4}$ for experimental data (■) at $Re \approx 9300$ (Schartman 2008), CCF (······), and our numerical simulations at $Re = 6200$: 3D (——), axisymmetric (- - - -) and noisy axisymmetric (— · —) cases. 3D effects are negligible compared to axisymmetric case both being slightly lower than experimental profile, and the best fit is achieved in the axisymmetric case with random noise perturbations applied to the surface of inner cylinder.

angular momentum leading to the zero angle between the jets and radius vector in accordance with the mechanism described above. Moreover, this angle is expected to be sensitive to the details of the flow in the vicinity of the ring boundary such as presence of gaps between rings, three-dimensionality, etc but it is likely to be adjusted with an appropriate choice of angular velocities of rings shifting the equilibrium points of local CCF balance and thus regulating the radial extent and radial linear momentum of the Ekman flows (cf Schartman 2008). In other words, the angular velocities of rings control EC through the net radial momentum after the collision of Ekman flows that sets the angle at which the jets are launched near the ring boundary $r = R_{12}$.

3.1.3. Summary on horizontal boundary effects. The CCF-like equilibrium between 'centrifugal' rotation and centripetal pressure gradient in cylindrical annulus is impossible to achieve experimentally due to the presence of the noslip horizontal boundaries. The rotation of these boundaries with either faster inner cylinder or slower outer cylinder creates the Ekman boundary layers with either angular momentum excess or deficit, correspondingly, and results in either outward or inward Ekman flows, respectively, that drive EC in the annulus. The splitting of the horizontal boundaries into independently rotating rings sets the CCF-like equilibrium points by matching locally to the CCF angular velocity, and the resulting angular momentum deficit or excess leads to the, correspondingly, inward or outward Ekman flows along the portions of the rings with radius, respectively, smaller or larger than the radius of these equilibrium points. The opposing Ekman flows along the rings collide near ring boundaries and launch the vertical jets at an angle presumably determined by the mismatch of their linear radial momentum. This angle is expected to be sensitive to the details of the flow structure inside and immediately near the gaps between rings,

the vertical alignment of the horizontal surfaces of the rings, etc and can be adjusted by changing the angular velocities of the rings (cf Schartman 2008).

3.2. Comparison with experiment

We have collaborated with Princeton MRI liquid gallium experiment group and conducted a comparison of our computations with their experimental results. Figure 5 shows the comparison of our numerical results for time-averaged azimuthal velocity in the case with lids at $Re = 6200$ with ideal CCF profile (dotted) and experimental measurements (squares) conducted by Schartman (2008) at $Re \approx 9300$. The solid line corresponds to the axisymmetric computation, while the fully 3D results are shown with the dashed line. We observe that at this Reynolds number ($Re \approx 6200$) 3D time-averaged azimuthal velocity is very close to the axisymmetric one, both of them being up to 15% lower than the experimental data. The difference in Reynolds number is expected to play only a minor role in this discrepancy.

The best fit of our (axisymmetric) computations (dashed–dotted line) with experimental data was realized when the boundary conditions (9) were perturbed with uniform random noise. The amplitude of the noise was 5% relative to the corresponding maxima of the axisymmetric solution without noise. The noise perturbation was applied for the part of the computational domain boundary of one spectral element long such that $R_1 \leqslant r < R_1 + L_g$ where $L_g = 0.0200$, which is less than twice of the non-dimensional width of the gap between the inner cylinder and inner ring in the Princeton experiment equal to 0.0114 or 1.5 mm (Schartman 2008).

The rationale behind the noise perturbation of the boundary conditions was an attempt to model the effect of the centrifugally unstable flow in the gap between the inner cylinder and inner ring. By an accident, boundary conditions
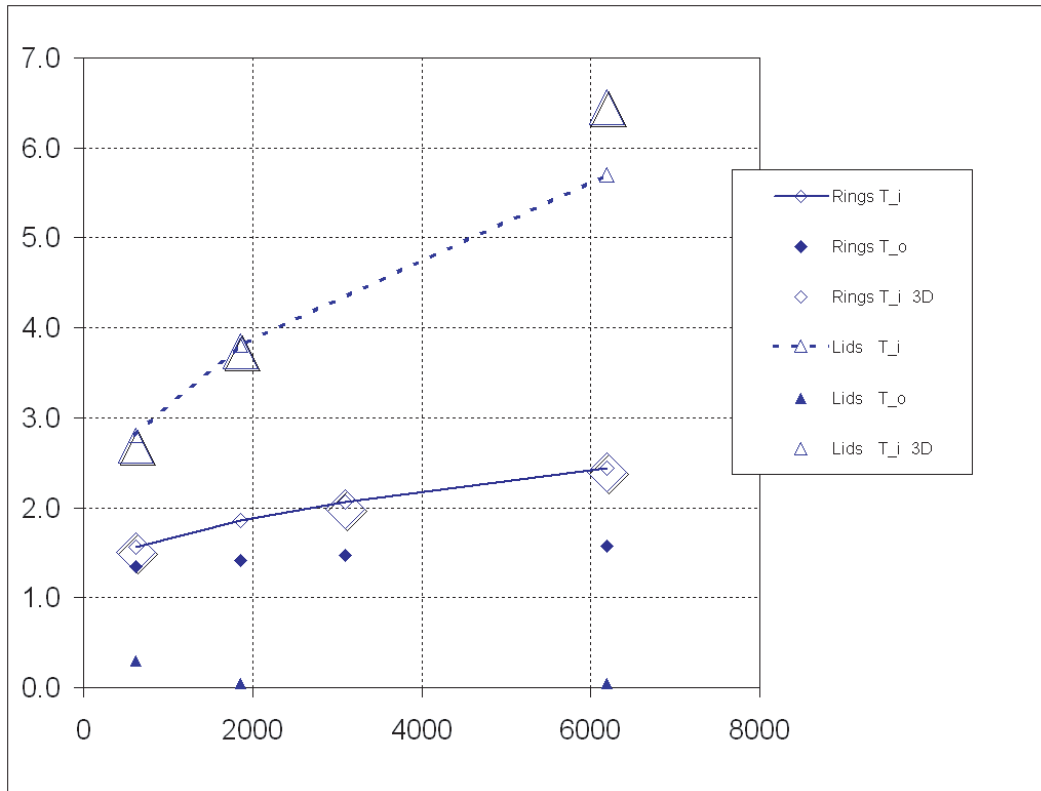
Figure 6. The magnitudes of normalized torques applied to the inner cylinder ($T_i = \mathcal{T}_1/\mathcal{T}_C$, open symbols) and the outer cylinder ($T_o = -\mathcal{T}_2/\mathcal{T}_C$, filled symbols) versus Reynolds number for the cases with rings (—◇— or ◆) and the cases with lids (···△··· or ▲) in axisymmetric cases, while the 3D data are plotted with large symbols. Being the sum of magnitudes of torques applied to the inner and outer cylinders, the net torque exerted on the horizontal boundaries in the case of rings is significantly less than that in the case of lids, making the former a closer approximation to the CCF for which the net torque on horizontal boundaries is zero.

on the inner cylinder surface ($r = R_1$) were also perturbed in this computation, which turned out to be the best fit with experimental data. The effect of this perturbation of the inner cylinder surface boundary condition may be similar to a random blowing. This leads us to believe that a combination of the effects due to a run-out of the inner cylinder and due to the centrifugally unstable flow in the gaps between the inner cylinder and inner ring may explain the discrepancy between the simulation and experiment (see also Schartman 2008).

Further work on comparison of the simulation with experiment is ongoing, and additional effort is needed to sort out the effects of run-out, centrifugally unstable flow in the gaps between cylinders and rings, vertical misalignment of horizontal surfaces of the rings, etc.

3.3. Torque and AMT

Also we have studied carefully the torque behavior and associated AMT in the hydrodynamical setup of the Princeton MRI liquid gallium experiment (Schartman 2008) as a baseline case for our study of MRI and MRI-driven turbulence. In order for the MRI experimental results to have a clear interpretation, the negative effects of the EC have to be minimized, and the torque amplification over the CCF torque $\mathcal{T}_C$ (15) with the increase of magnetic field can be linked directly to MRI enhancement of AMT. Therefore, the understanding of the torque behavior and AMT in the baseline cases of hydrodynamical flow cannot be overstated.

An application of torque to the inner cylinder results in a flow that transports the angular momentum outward and attempts to reach a shear-free solid body rotation with a constant angular velocity. If the angular velocities of other boundaries are different from that of the inner cylinder, the resulting shear has to be maintained by application of torques to the boundaries in order to keep the rotation rates steady. In the context of the MRI study, the primary interest is in the transport of the angular momentum from the inner to outer cylinder in the centrifugally stable regime and, as shown below, in the minimization of EC and, hence, in the reduction of the net contribution of torques exerted on the horizontal boundaries. Since the sum of all torques applied to the boundaries reflects the time increase of the interior angular momentum, this contribution from the horizontal boundaries is equal to the sum of torques applied to the cylinders in a steady state and has to be minimized for the successful MRI experiment. Note that in the case of unsteady flow, the time-averaged torques are used when the statistically steady state is reached.

Figure 6 shows the Reynolds number dependence of magnitudes of steady/time-averaged torque relative to the ideal CCF torque $\mathcal{T}_C$ (15) that has to be applied to inner and outer cylinders, $T_i = \frac{\mathcal{T}_1}{\mathcal{T}_C}$ (open symbols) and $T_o = \frac{-\mathcal{T}_2}{\mathcal{T}_C}$ (filled symbols), respectively, in order to keep constant boundary angular velocities (table 1). Being equal to unity for the case with periodic boundary conditions (CCF), the torque magnitudes are shown for the cases with rings (open diamonds
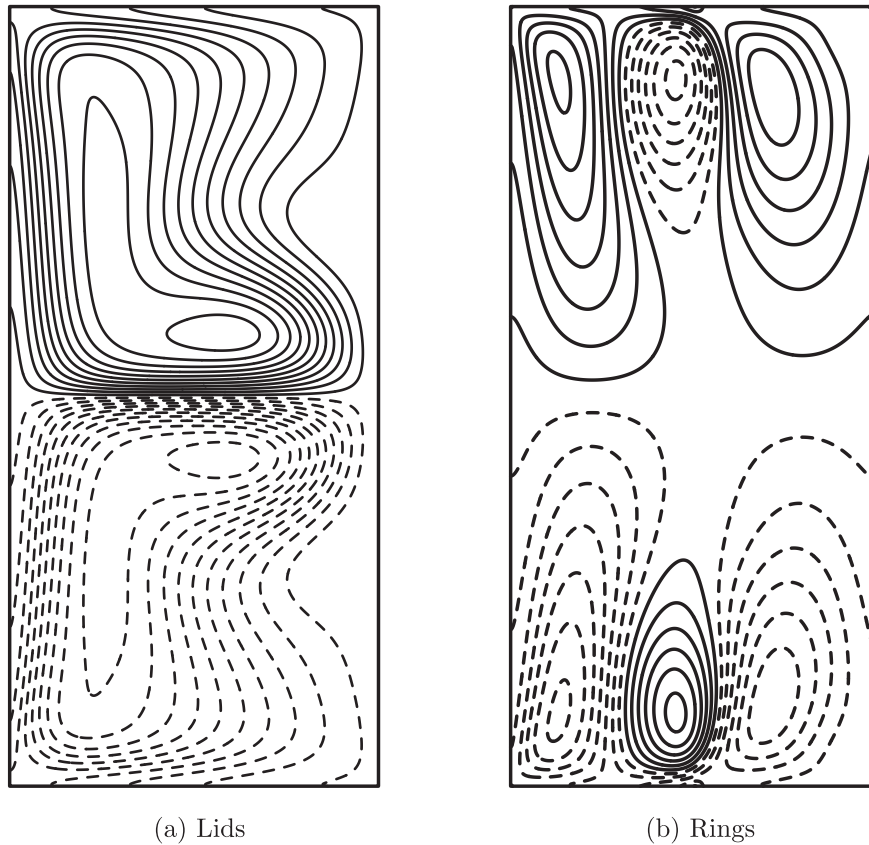
(a) Lids

(b) Rings

Figure 7. Steady-state contour lines of effective angular momentum flux function $\tilde{\Psi}$ for the case of $Re = 620$ with lids in the range from -3.30 to 3.30 in the increment of 0.31 (a) and with rings in the range from -1.35 to 1.35 in the increment of 0.21 (b). In the case of lids, most of the flux lines that originate from inner cylinder terminate at horizontal boundaries as opposed to the case of rings where they end up mostly at the outer cylinder which is similar to the CCF angular momentum transport between the cylinders.

with solid lines and filled diamonds) and lids (open triangles with dotted lines and filled triangles). All results are obtained in axisymmetric computations except for the data plotted with large open symbols that show the results of fully 3D computations. Note that being zero in the ideal CCF, the difference between the torques applied to the inner and outer cylinders shown by open and closed symbols, respectively, corresponds to the sum of torques exerted on the fluid next to the horizontal boundaries

$$T_i - T_o = (\mathcal{T}_1 + \mathcal{T}_2)/\mathcal{T}_C$$

due to zero net torque in steady/statistically steady state. Evidently, the setup with rings has the advantage of a smaller contribution to the net torque from the horizontal boundaries and of a smaller difference between inner and outer cylinder torque magnitudes over the setup with lids where EC is undisturbed. We also observe that in the range of Reynolds numbers considered the flow makes a transition from steady axisymmetric solution at $Re = 620$ to the unsteady one at $Re = 6200$ with small 3D effects. Being more significant in the case with lids, three-dimensionality is expected to play an increasing role with the further increase of Reynolds number.

In order to illustrate spacial variations of AMT, we have computed an effective angular momentum flux function defined in appendix B by analogy with a streamfunction. The contours of the effective flux function show the (flux) lines along which the angular momentum is transported, and the

difference between the values of the flux function at two points gives the total flux across the segment of conical or cylindrical surfaces on which these points lie. Figure 7 shows steady-state contour lines of constant increment for effective angular momentum flux function $\tilde{\Psi}$ (B.12) for the case of $Re = 620$ with lids (a) and rings (b). For comparison, we note that the flux lines of (purely viscous) AMT for the ideal CCF (12) are the straight lines from the inner to outer cylinder along $z =$const. Despite the fact that in both cases only a single line of $\tilde{\Psi} = 0$ (i.e. line of symmetry) is the same as in the CCF case, the case with rings exhibits the similar transport of angular momentum along the flux lines that mostly originate at the inner cylinder and terminate at the outer cylinder in contrast with the termination of the flux lines at the lids. The latter indicates that in the cases with lids, the angular momentum transport is mostly between the inner cylinder and the horizontal boundaries, contrary to more desirable CCF-like transport between the cylinders observed in the cases with rings. Also note that the similarity between the shape of the flux lines away from the boundaries in figure 7 and the shape of vorticity contour lines and poloidal vector lines in figure 4 can be explained through creation of strong V_r and V_z components of velocity due to Ekman flows, which affects AMT flux through advective contributions F_{rz}^a and F_{zz}^v, respectively, given by relations (B.5) and (B.6).

In summary, if the ultimate objective is to achieve the flow with AMT as close to the ideal CCF as possible, the

design with rings seems to have an advantage over the setup with lids.

4. Conclusion and future work

In this paper, we have presented axisymmetric and fully 3D Navier–Stokes calculations of CCF in a cylindrical annulus as the first step in our study of MRI and MRI-driven turbulence. Inspired by Princeton MRI liquid gallium experiment, we have computed the flow field in their experimental setup for realistic horizontal boundary conditions of 'lids' and 'rings' with the increase of Reynolds number through the onset of unsteadiness and three-dimensionality. The presented analysis of the flow field and AMT allowed us to propose an explanation of the mechanism that determines the fate of the boundary flows and EC as a result of a competition between the effects of 'centrifugal' rotation and pressure gradient set by rotation of, respectively, horizontal surfaces and bulk of the flow. In particular, with the appropriate choice of rotation rates of the horizontal rings that control an angle at which the vertical jets are launched near the ring boundaries, EC can be greatly diminished and CCF-like flow can be restored being more appropriate for the further experimental studies of MRI saturation and enhanced AMT. In addition, our numerical results compare favourably with the experimental data with the maximum deviation below 15% being considerably smaller in the cases with 'noisy' boundary conditions. Future work should therefore involve higher Reynolds number computations with even more detailed modelling of experimental geometry that includes among others the effects of run-out of the inner cylinder, finite gaps between the cylinders and rings, and vertical misalignment of horizontal surfaces of the rings.

Appendix A. Traditional explanation of EC

Here we would like to comment that the traditional explanation of Ekman flows and circulation involves a balance between Coriolis and viscous forces in Ekman layers along rotating stressed boundary as viewed from a uniformly rotating reference frame (see Batchelor 1967, Greenspan 1968). As we show below, this balance of Coriolis and viscous forces holds, for instance, in the case of a bulk flow outside the Ekman layers that is close to the state of solid body rotation at, say, angular velocity of Ω_2, when the centripetal pressure gradient and centrifugal forces cancel each other:

$$ p \sim \frac{1}{2}\Omega_2^2 r^2, \qquad r\Omega_2^2 + \frac{\partial p}{\partial r} \sim 0 \qquad (A.1) $$

(to the order of Ekman number $E = \frac{\nu}{\Delta\Omega L^2} \sim \frac{1}{Re}$, see Greenspan 1968) and the Coriolis force is solely responsible for the Ekman flow. In other flows such as those considered in this paper, a contribution of the 'centrifugal' rotation to the Ekman flow does not reduce solely to the Coriolis force but also includes the effects of centrifugal forces. Indeed, for the flow description in the non-inertial reference frame that rotates with constant angular velocity of the noslip boundary of the 'lids' $\mathbf{\Omega_2} = \Omega_2\mathbf{e_z}$, the centrifugal and Coriolis body forces have to be added to the right-hand side of equations (3)–(5),

$$ \boldsymbol{f} = -\,\boldsymbol{\Omega_2} \times (\boldsymbol{\Omega_2} \times \boldsymbol{r}) - 2\,\boldsymbol{\Omega_2} \times \boldsymbol{u}, $$
$$ f_{\mathrm{r}} = \Omega_2^2 r + 2\,\Omega_2\,u_\Theta, \qquad (A.2) $$

along with the replacement of the inertial frame velocity **V** with the velocity in the non-inertial rotating reference frame **u** leading to the following radial momentum equation in, e.g., the case of axisymmetry ($\frac{\partial}{\partial\theta} = 0$):

$$ \frac{\partial u_{\mathrm{r}}}{\partial t} + \boldsymbol{u}\cdot\boldsymbol{\nabla} - \frac{u_\Theta^2}{r} = \Omega_2^2 r + 2\,\Omega_2\,u_\Theta + \frac{1}{Re}\left[\triangle_{(r,z)}u_{\mathrm{r}} - \frac{u_{\mathrm{r}}}{r^2}\right] - \frac{\partial p}{\partial r} $$

or

$$ \frac{\partial u_{\mathrm{r}}}{\partial t} = \Omega_2^2 r + \left(2\,\Omega_2\,u_\Theta + \frac{u_\Theta^2}{r}\right) - \frac{\partial p}{\partial r} + \frac{1}{Re}\frac{\partial^2 u_{\mathrm{r}}}{\partial r^2} + \cdots. \qquad (A.3) $$

Let us now compare this relation with equation (16) where we expand the 'centrifugal' term $\Omega^2 r$ in powers of azimuthal velocity deviation from the state of solid body rotation of the lids, $U_\theta = V - r\Omega_2$:

$$ \Omega^2 r = \frac{V_\theta^2}{r} = \frac{(r\Omega_2 + U_\theta)^2}{r} = \Omega_2^2 r + \left(2\,\Omega_2\,U_\theta + \frac{U_\theta^2}{r}\right). \qquad (A.4) $$

Therefore, the equation of radial momentum balance (16) rewritten with the expansion (A.4) coincides exactly with equation (A.3) in the case of axisymmetric flow when the difference between V_{r} and u_{r} and between U_θ and u_Θ disappears due to the relationship between velocities in the inertial and non-inertial reference frames:

$$ \mathbf{V}(r, \theta, z, t) = r\,\Omega_2\,\mathbf{e_\Theta} + \mathbf{u}(r, \Theta = \theta + \Omega_2 t, z, t) $$

or

$$ \mathbf{V}(r, z, t) = r\,\Omega_2\,\mathbf{e_\theta} + \mathbf{u}(r, z, t). \qquad (A.5) $$

In the particular case of flows that are close to solid body rotation when considered in this description (A.3) equivalent to our earlier framework (16), the contribution of the centrifugal and pressure gradient forces cancels out (A.1), resulting in the steady-state balance of the Coriolis and viscous forces,

$$0 = 2\,\Omega_2\,u_\Theta + \frac{1}{Re}\frac{\partial^2 u_r}{\partial r^2} + \cdots, \qquad (A.6)$$

where we omitted higher order terms including $\frac{u_\Theta^2}{r} \ll 2\,\Omega_2\,u_\Theta$ away from the axis of rotation $r=0$ due to vanishing u_Θ at the noslip boundary. In the more general case, the additional contributions of the centrifugal forces $\Omega_2^2 r$ and $\frac{u_\theta^2}{r}$ to the Ekman flows have to be considered as being a part of the 'centrifugal' term $\Omega^2 r$ (16, A.3) that is balanced by centripetal pressure gradient and viscous forces in the Ekman flows along the lids that drive EC in the cylindrical annulus.

Appendix B. Angular momentum flux and flux function

Let us take the axisymmetric version of azimuthal momentum equation (4) with viscosity ν instead of $\frac{1}{Re}$ and rewrite it in terms of conservation of axial angular momentum $\mathcal{L} = r V_\theta$. The summation of the axisymmetric versions of equations (4) and (6) multiplied by factors $-r$ and $r V_\theta$, correspondingly, gives

$$-\frac{\partial}{\partial t}(r V_\theta) = -r\left[-V_r\frac{\partial V_\theta}{\partial r} - V_z\frac{\partial V_\theta}{\partial z} - \frac{V_r V_\theta}{r}\right.$$
$$\left. + \nu\left(\frac{\partial^2 V_\theta}{\partial r^2} + \frac{1}{r}\frac{\partial V_\theta}{\partial r} + \frac{\partial^2 V_\theta}{\partial z^2} - \frac{V_\theta}{r^2}\right)\right]$$
$$+ r V_\theta\left[\frac{\partial V_r}{\partial r} + \frac{\partial V_z}{\partial z} + \frac{V_r}{r}\right]$$

$$= \left[r V_r\frac{\partial V_\theta}{\partial r} + r V_z\frac{\partial V_\theta}{\partial z} + V_r V_\theta - \nu\left\{ r\frac{\partial^2 V_\theta}{\partial r^2}\right\}\right.$$
$$\left. -\nu r\left(\frac{1}{r}\frac{\partial V_\theta}{\partial r} - \frac{V_\theta}{r^2}\right) - \nu r\frac{\partial^2 V_\theta}{\partial z^2}\right]$$
$$+ \left[r V_\theta\frac{\partial V_r}{\partial r} + r V_\theta\frac{\partial V_z}{\partial z} + V_r V_\theta\right]$$

$$= \frac{\partial[r V_r V_\theta]}{\partial r} + \frac{\partial[r V_\theta V_z]}{\partial z} + V_r V_\theta$$
$$-\nu\left\{\frac{\partial}{\partial r}\left[r\frac{\partial V_\theta}{\partial r}\right] - \frac{\partial V_\theta}{\partial r}\right\} - \nu r\frac{\partial}{\partial r}\left(\frac{V_\theta}{r}\right)$$
$$+ \frac{\partial}{\partial z}\left[-\nu r\frac{\partial V_\theta}{\partial z}\right]$$

$$= \frac{\partial}{\partial z}\left[r V_\theta V_z - \nu r\frac{\partial V_\theta}{\partial z}\right]$$
$$+ \frac{\left[r V_r V_\theta - \nu r^2\frac{\partial}{\partial r}\left(\frac{V_\theta}{r}\right)\right]}{r} + \frac{\partial}{\partial r}[r V_r V_\theta]$$

$$-\nu\left\{\frac{\partial}{\partial r}\left[\left(r^2\frac{\partial}{\partial r}\left(\frac{V_\theta}{r}\right) + V_\theta\right) - V_\theta\right]\right\}$$

$$= \frac{\partial}{\partial z}\left[r V_\theta V_z - \nu r\frac{\partial V_\theta}{\partial z}\right]$$
$$+ \frac{\left[r V_r V_\theta - \nu r^2\frac{\partial}{\partial r}\left(\frac{V_\theta}{r}\right)\right]}{r}$$
$$+ \frac{\partial}{\partial r}\left[r V_r V_\theta - \nu r^2\frac{\partial}{\partial r}\left(\frac{V_\theta}{r}\right)\right]$$

$$= \frac{1}{r}\frac{\partial}{\partial r}\left(r\left[r V_r V_\theta - \nu r^2\frac{\partial}{\partial r}\left(\frac{V_\theta}{r}\right)\right]\right)$$
$$+ \frac{\partial}{\partial z}\left(r V_\theta V_z - \nu r\frac{\partial V_\theta}{\partial z}\right). \qquad (B.1)$$

The above equation (B.1) reflects the conservation of the axial or z-component of angular momentum and can be condensed to

$$\frac{\partial}{\partial t}(r V_\theta) + \frac{1}{r}\frac{\partial}{\partial r}(r F_{rz}) + \frac{\partial F_{zz}}{\partial z} = 0 \qquad (B.2)$$

or

$$\left(\frac{\partial}{\partial t}(\boldsymbol{r}\times\boldsymbol{V}) + \nabla_{(r,z)}\cdot\mathbf{F}\right)_z = 0, \qquad (B.3)$$

where total angular momentum flux tensor $\mathbf{F}$ and its components F_{rz} and F_{zz} are given for axisymmetric flows by

$$\mathbf{F} = \mathbf{F^a} + \mathbf{F^v}, \qquad (B.4)$$

$$F_{rz}^a = r V_r V_\theta, \qquad (B.5)$$

$$F_{zz}^a = r V_\theta V_z, \qquad (B.6)$$

$$F_{rz}^v = -\nu r^2\frac{\partial}{\partial r}\left(\frac{V_\theta}{r}\right) = -r\tau_{r\theta}, \qquad (B.7)$$

$$F_{zz}^v = -\nu r\frac{\partial V_\theta}{\partial z} = -r\tau_{z\theta}, \qquad (B.8)$$

where superscript a and v denote an advective and a viscous contributions to the total flux of angular momentum, and $\tau_{r\theta}$ and $\tau_{z\theta}$ are components of the stress tensor $\boldsymbol{\tau}$.

By analogy with poloidal streamfunction ψ that satisfies the axisymmetric version of continuity equation (6) due to, e.g., a definition

$$V_r = \frac{\partial\psi}{\partial z}, \qquad V_z = -\frac{1}{r}\frac{\partial(r\psi)}{\partial r}, \qquad (B.9)$$

an angular momentum flux function $\Psi(r,z)$ for steady flows can be introduced to satisfy the steady version of equation (B.2):

$$F_{rz} = \frac{\partial\Psi}{\partial z}, \qquad F_{zz} = -\frac{1}{r}\frac{\partial(r\Psi)}{\partial r}. \qquad (B.10)$$

As the lines of constant value of poloidal streamfunction ψ are lines of constant poloidal flow rate with poloidal velocity vector being tangent to these streamlines, the lines of constant total angular momentum flux function Ψ are the flux lines along which angular momentum is transported, and the difference between these values at any two points gives the total flux of angular momentum transferred across the line that joins these points. Note that in the case of unsteady flow, the time-averaged quantities can be used in statistically steady state instead of instantaneous ones. Also note that similar to the streamfunction, the flux function Ψ as a solution of equations (B.10) is defined up to a constant. We have used the point of half-height on the inner cylinder as a zero value for the flux function

$$\Psi\left(r = R_1, z = \frac{H}{2}\right) = 0 \tag{B.11}$$

and, for convenience, we define the effective flux function $\tilde{\Psi}$ as a flux function Ψ multiplied by circumference $2\pi r$ and scaled by the ideal CCF torque $\mathcal{T}_C$ (15)

$$\tilde{\Psi}(r, z) = \frac{2\pi r}{\mathcal{T}_C} \Psi(r, z). \tag{B.12}$$

Finally, due to multiplication of flux function Ψ by r, the difference in effective flux function $\tilde{\Psi}$ between two points gives the total flux of angular momentum across the conical or cylindrical surface on which these points lie. Thus, in the case of e.g. the inner and outer cylinder, it can be shown

that torques $\mathcal{T}_1$ and $\mathcal{T}_2$ scaled by the ideal CCF torque $\mathcal{T}_C$ are given by

$$\begin{aligned}
\frac{\mathcal{T}_1}{\mathcal{T}_C} &= \tilde{\Psi}(R_1, H) - \tilde{\Psi}(R_1, 0), \\
\frac{-\mathcal{T}_2}{\mathcal{T}_C} &= \tilde{\Psi}(R_2, H) - \tilde{\Psi}(R_2, 0).
\end{aligned} \tag{B.13}$$

Similar expressions hold for the torques applied to the horizontal surfaces.

References

Alpher R A and Herman R 1960 *Am. J. Phys.* **28** 748

Balbus S A 2003 *Ann. Rev. Astron. Astrophys.* **41** 555–97

Batchelor G K 1967 *An Introduction to Fluid Dynamics* (Cambridge: Cambridge University Press)

Burin M J, Ji H, Schartman E, Cutler R, Heitzenroeder P, Liu W, Morris L and Raftopolous S 2006 *Exp. Fluids* **40** 962–6

Fischer P F, Loth F, Lee S E, Lee S W, Smith D S and Bassiouny H S 2007 *Comput. Meth. Appl. Mech. Eng.* **196** 3049–60

Fischer P F, Obabko A and Cattaneo F 2008 *J. Sci. Comput.* in preparation

Greenspan H P 1968 *The Theory of Rotating Fluid* (Cambridge: Cambridge University Press)

Ji H, Burin M, Schartman E and Goodman J 2006 *Nature* **444** 343–6

Kageyama A, Ji H, Goodman J, Chen F and Shoshan E 2004 *J. Phys. Soc. Japan* **73** 2424–37

Rosner R, Rüdiger G and Bonanno A (eds) 2004 *MHD Couette Flows: Experiments and Models* (*American Institute of Physics Conf. Proc. 733*) (New York: AIP)

Schartman E 2008 Laboratory study of angular momentum transport in a rotating shear flow *PhD Thesis* University of Princeton